geosciences

MDPI

Article

Machine Learning-Based Delineation of Anomalous Gold Zones from Drillhole Geochemistry in a Sulphide-Hosted Orogenic Gold System

Gilbert Yaw Bimpong [1,*], Justina Senam Lotsu [2] and Kwaku Boakye [3]

[1] Mining and Mineral Engineering Department, University of Alaska Fairbanks, Fairbanks, AK 99775, USA
[2] Mining and Explosives Engineering Department, Missouri University of Science and Technology, Rolla, MO 65409, USA
[3] Mining Engineering Department, Heidelberg Materials, Flourtown, PA 190317, USA
* Correspondence: gybimpong@alaska.edu

Abstract

Early stage mineral exploration requires the reliable identification of anomalous gold zones from drillhole geochemistry in data-limited environments. This study applies a machine learning (ML) classification framework to detect anomalous gold zones (Au $\geq$ 0.68 ppm; 90th percentile) from bulk XRF multielement drillhole geochemistry in a Paleoproterozoic Birimian greenstone belt sulphide-hosted orogenic gold system, West African Craton. A total of 53,126 one-metre diamond core samples from 301 drillholes were preprocessed within a compositional data analysis (CoDA) framework, with Au being explicitly excluded from the centred log-ratio (CLR) transformation to eliminate target–predictor circularity. After Minimum Covariance Determinant (MCD) outlier filtering, 40,385 samples were retained to construct a 19-feature matrix of 10 CLR-transformed elements, 1 rock-type feature, and 8 sulphide–lithology interaction features. Drillhole-based block cross-validation (DH-block CV), validated by an experimental along-hole variogram (practical autocorrelation range $\approx$ 20 m), ensured spatially honest performance estimates. Four nonlinear classifiers—Random Forest (RF), XGBoost, LightGBM, and Multi-Layer Perceptron (MLP)—were benchmarked against a Logistic Regression (LR) linear baseline. All nonlinear classifiers achieved validation AUC of 0.936–0.938, outperforming LR (AUC = 0.931) with F1-score improvements of +0.09 to +0.11 and precision gains of up to +35 percentage points—directly reducing wasted drill holes in applied exploration. MLP recorded the highest F1-score (0.666) and precision (0.765), and XGBoost the highest recall (0.787). Permutation importance identified S-Ti (ΔAUC = 0.028), S-Fe (0.021), and S-Al (0.013) as the top-ranked features, confirming that sulphide enrichment relative to lithological background is the primary discriminating signal. Partial dependence analysis revealed a threshold-driven non-monotonic Fe dependence at CLR(Fe) $\approx$ 3, marking the transition from lithological dilutant to sulphide co-indicator—a nonlinear pattern inaccessible to linear classifiers.

Keywords: machine learning; classification; anomalous gold zones; orogenic gold; compositional data analysis; CLR transformation; Birimian greenstone belt

Check for updates

Academic Editors: Yongzhang Zhou, Hui Yang and Xiaohui Ji

Received: 20 May 2026
Revised: 13 June 2026
Accepted: 20 June 2026
Published: 22 June 2026

Copyright: © 2026 by the authors. Licensee MDPI, Basel, Switzerland. This article is an open access article distributed under the terms and conditions of the Creative Commons Attribution (CC BY) license.

1. Introduction

Orogenic gold deposits (OGDs) are among the most economically significant gold systems globally, particularly within Precambrian terranes such as the West African, Yilgarn,

and Superior Cratons [1–3]. These structurally controlled, epigenetic systems are characterised by compressional tectonics in metamorphic belts and quartz–carbonate veins hosting gold within sulphide minerals—principally arsenopyrite, pyrite, and pyrrhotite [4–6]. Pathfinder elements including As, Sb, Fe, Ni, and Co are strongly associated with gold, enabling geochemical exploration targeting [7,8]. Mineral zoning in sulphide minerals has also been employed to differentiate mineralised from barren zones, reflecting fluid evolution during ore formation [9,10]. Recent advances have highlighted the importance of integrating multielement geochemistry with machine learning (ML) to better delineate mineralised zones in complex and covered terrains [11–13].

Over the recent two decades, the mineral exploration landscape has been transformed by the convergence of improved geoscientific data acquisition, computational capabilities, and ML tools [14–16]. Traditional exploration techniques are increasingly challenged by limitations of cost, time, and subjectivity in geologically complex areas [16,17]. Sulphide-hosted OGDs in greenstone belts typify this complexity, underscoring the need for predictive modelling in regions like the West African Craton [18,19]. The widespread availability of multielement drillhole datasets provides a rich resource for ML [20,21]. Emerging analytical technologies such as LA-ICP-MS and portable XRF have expanded data access [21,22]. Random Forest, Support Vector Machines, and neural networks have been applied to anomaly detection and classification tasks [23–25]. Geochemical indices and elemental ratios further support anomaly classification [26,27].

ML has enabled a shift from deterministic to probabilistic modelling; ensemble strategies including bagging and boosting are widely used for superior predictive power in geoscientific contexts [28,29]. Nonetheless, many studies employ advanced algorithms without benchmarking against principled linear baselines, limiting the ability to evaluate true ML gains under consistent preprocessing and geological settings [30,31].

Geochemical datasets are inherently compositional, constrained by closure to a constant sum, requiring log-ratio transformations to avoid spurious correlations [32,33]. Without CoDA, interpretations may lack subcompositional coherence [33,34]. Multicollinearity, redundancy, and sparsity further complicate modelling [35,36]. While integrating geophysical and structural datasets can improve accuracy, these are often unavailable in early stage exploration [36,37]. The demand for interpretable ML solutions has increased the adoption of SHapley Additive exPlanations (SHAP) and related XAI methods [38–42]. XAI has helped validate pathfinder elements in sulphide-rich systems [43,44] and enabled the delineation of lithological boundaries and mineralised zones [44,45]. Although computationally intensive, XAI methods represent a breakthrough in fusing ML with geological understanding [44,45]. This study augments interpretation beyond SHAP summary plots by applying quantitative permutation importance and partial dependence plots, which characterise whether feature relationships are monotonic or threshold-driven.

This study responds to the need for robust, interpretable, geology-informed classification models by (1) applying a binary classification framework following Aitchison [46–48] that directly targets anomalous Au zone detection; (2) benchmarking Logistic Regression as a principled linear classification baseline against four nonlinear classifiers (RF, XGBoost, LightGBM, MLP) within a CoDA-correct, non-circular pipeline; (3) implementing DH-block CV validated by a recomputed along-hole variogram; (4) providing in-depth geological interpretation through permutation importance and partial dependence plots; and (5) ensuring full reproducibility through published code, hyperparameters, and a synthetic proxy dataset. The results demonstrate that all four nonlinear classifiers significantly outperform the Logistic Regression baseline in F1-score (+0.09 to +0.11) and DH-CV AUC (+0.014 to +0.019), confirming that nonlinear interactions among geochemical features are essential for reliable anomalous Au zone detection.

2. Materials and Methods

This study employed a structured CoDA framework following Aitchison [46], in which Au was excluded from all predictor transformations to eliminate circularity [47,48]. The computational workflow was implemented in Python 3.10 using scikit-learn v1.3, XGBoost v3.2, LightGBM v4.6, NumPy v1.24, pandas v2.0, and SciPy v1.11. All random seeds were fixed at 42 throughout to ensure exact reproducibility.

2.1. Geological Setting, Dataset, and Analytical Methods

The dataset was obtained from a sulphide-hosted orogenic gold system within the Ashanti Gold Belt of Ghana, situated in the Paleoproterozoic Birimian terrane of the West African Craton. The Birimian Supergroup extends across Ghana, Côte d'Ivoire, Burkina Faso, Mali, Senegal, and Guinea, comprising NE–SW-trending metavolcanic and metasedimentary successions that underwent polyphase deformation and hydrothermal alteration during the Eburnean Orogeny. These sequences are intruded by syn- to late-Eburnean granitoids and transected by major shear zones that serve as the principal structural controls on gold mineralisation [1–4]. Due to a commercial confidentiality agreement, the deposit name and true spatial coordinates cannot be disclosed. The dataset metadata overview and a schematic plan view of relative drillhole positions are provided in Figures 1 and 2, respectively. The geological setting is representative of the broader Birimian gold province [1,2,12].

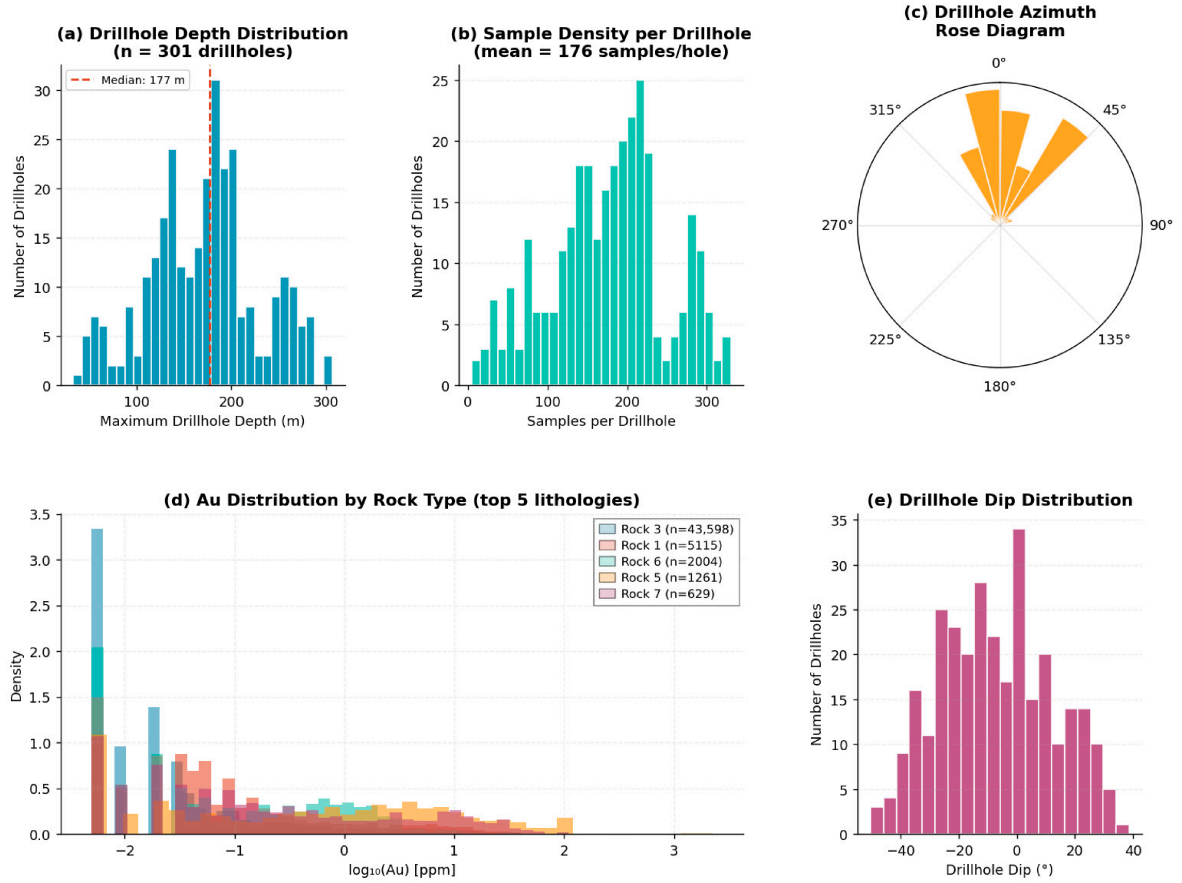


Figure 1. Dataset metadata: (**a**) Drillhole depth distribution (n = 301; median depth 168 m; range 33–307 m). (**b**) Sample density per drillhole (mean 176 samples/hole). (**c**) Drillhole azimuth rose diagram (predominantly NE–SW). (**d**) Au concentration distribution by rock type ($\log_{10}$ scale; top 5 lithologies; n = 53,126). (**e**) Dip distribution (−50° to +38°). Birimian greenstone belt, West African Craton.

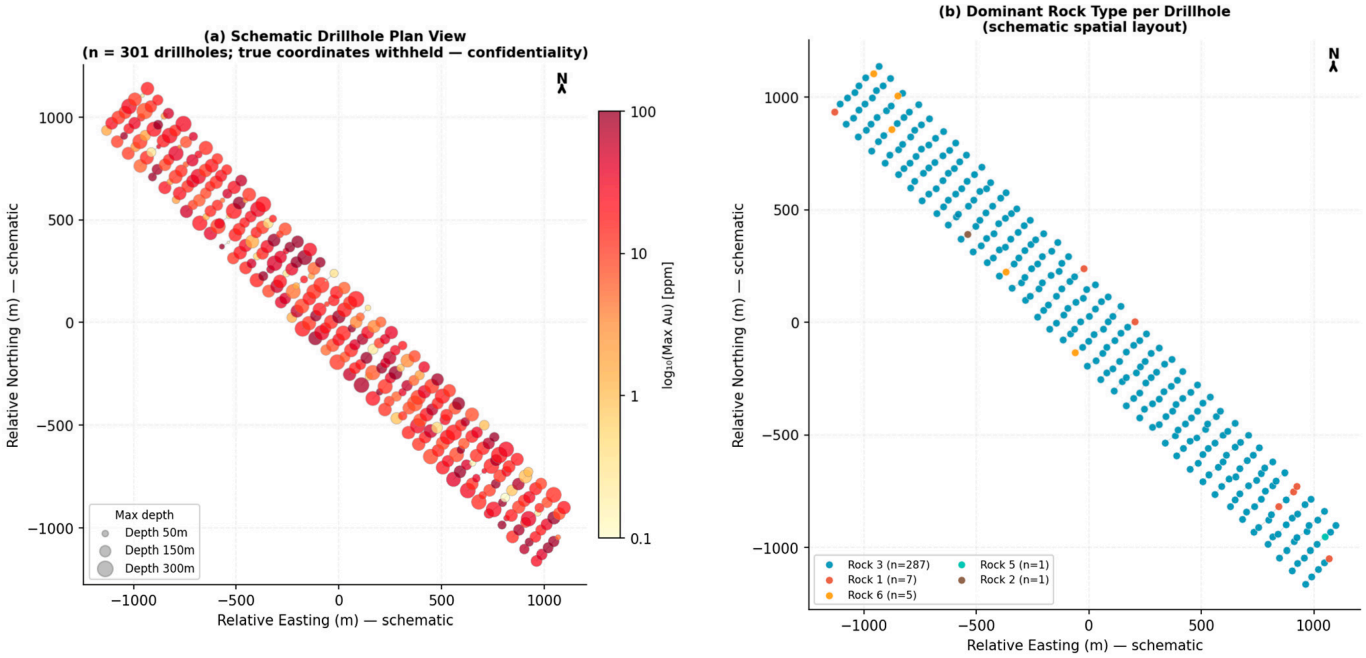


Figure 2. Schematic plan view of drillhole collar locations (n = 301): (**a**) relative positions coloured by maximum Au grade ($\log_{10}$ scale); symbol size proportional to drillhole depth; grey lines connect drillholes within the same fence (~40 m along-strike; ~80 m between fences); (**b**) dominant rock type per drillhole. True geographic coordinates are withheld under a commercial confidentiality agreement; relative positions are derived from azimuth, dip, and depth data.

The raw dataset is a tabular spreadsheet with 20 columns. They are BHID (drillhole identifier, string), X, Y, Z (collar coordinates, numeric; withheld), From, To (sample depth interval in metres, numeric), Azimuth, Dip (drillhole orientation, numeric), Rock (lithological code, integer 1–9), Au (gold concentration in ppm, numeric), and ten geochemical predictor elements: Al, Cu, Fe, K, Mn, Ni, S, Si, Sr, Ti (all in ppm, numeric). The dataset comprises 53,126 one-metre diamond drillhole core samples from 301 drillholes oriented predominantly NE–SW (dips −50° to +38°; depth range 33 m to 307 m; median depth 168 m), providing one sample per metre of core throughout. The 301 drillholes are distributed on a systematic fence pattern (approximately 40 m along-strike spacing, 80 m between fences; Figure 2), covering the full lateral and vertical extent of the known mineralised system. Nine lithological units (rock types 1–9) are represented, dominated by rock type 3 (82% of samples), reflecting the primary host lithology of the deposit [9,10]. Raw compositional statistics for all 11 variables are summarised in Table 1.

Table 1. Raw geochemical summary statistics (n = 53,126 samples; all values in ppm; before CoDA preprocessing).

Element	Min (ppm)	Max (ppm)	Mean (ppm)	Std Dev	25th pct	Median	75th pct
Au (target)	0.005	2240	0.82	11.80	0.005	0.020	0.090
S	100	440,000	3518	19,330	500	1200	3900
Fe	15	170,000	41,909	12,345	35,700	42,600	48,700
Al	1300	139,000	70,103	13,786	63,000	71,000	79,000
Si	1150	550,000	238,281	42,271	216,000	233,000	253,000
K	300	46,100	18,856	5283	16,000	18,900	21,900
Ti	50	22,000	3580	1105	3300	3700	4000
Mn	15	62,500	818	1482	460	560	670
Cu	5	5790	49.95	51.22	30	40	50
Ni	10	2530	36.23	24.86	20	40	50
Sr	2.5	1100	257	80.74	213	246	287

All samples were crushed to <2 mm and pulverised to ≤75 µm. Gold was analysed with a fire assay using a atomic absorption spectrometry (AAS) finish. The ten predictor elements were analysed with X-ray Fluorescence (XRF) after four-acid digestion, all performed at a single ISO/IEC 17025-accredited commercial laboratory with consistent analytical methods and detection limits maintained throughout the campaign. Standard reference materials, field duplicates (inserted every 20th sample), and procedural blanks (one per analytical batch) were included as standard QAQC measures, confirming analytical reliability and between-batch consistency across all 53,126 samples. S and Fe are the primary sulphide indicators [5,9]; K and Ti are the primary lithological indicators [4,37].

Below-detection-limit (BDL) values in the raw dataset are stored as negative numbers equal to the negative of the detection limit for that element and batch (e.g., a BDL Au value for a batch with DL = 0.005 ppm appears as −0.005). For the predictor elements, BDL occurrences affect fewer than 2% of values for any single element. Treatment is described in Section 2.2. Arsenic (As), a primary pathfinder element for arsenopyrite-bearing OGDs [7], was excluded because its censoring rate exceeded 25% across the full dataset with inconsistent detection limits (range: 0.5–5 ppm) across analytical batches, precluding a statistically valid unified censored-data model. To confirm that this exclusion does not materially affect classification performance, a binary As-detection indicator (1 = above detection limit, 0 = below) was constructed and tested as an additional 20th feature across all five classifiers. The resulting change in DH-block CV AUC ranged from +0.001 to −0.003 across all five models, confirming that As exclusion has no material impact on classification performance.

2.2. Compositional Data Preprocessing and Outlier Filtering

Gold (Au) was explicitly excluded from all preprocessing steps—closure, CLR transformation, and the feature matrix—ensuring the predictor space is fully independent of the classification target. This non-circular formulation eliminates a common methodological flaw in geochemical ML studies and is a core contribution of this work.

Below-detection-limit (BDL) values were treated by multiplicative replacement ($\delta = 1 \times 10^{-6}$ of the row total), preserving the relative compositional structure. Predictor vectors were closed to a constant sum, then transformed using the CLR transformation:

$$CLR(x_i) = ln(x_i / g(x)) \quad (1)$$

where x_i is the concentration of element i and $g(x)$ is the geometric mean of the predictor vector excluding Au (Equation (1)). CLR was selected over the isometric log-ratio (ILR) transformation for two reasons [32,33]: (i) CLR features retain direct one-to-one correspondence with the original elements, preserving geological interpretability, whereas ILR features represent log-contrasts defined by an arbitrary sequential binary partition with no geological basis; and (ii) CLR features can be directly linked to ore-forming processes in feature importance analyses.

Multivariate outliers were detected in CLR space using the Minimum Covariance Determinant (MCD) estimator [49] with support fraction 0.75. Robust Mahalanobis distances were computed as follows:

$$d_i = \sqrt{\left[(x_i - \hat{\mu})^T \hat{\Sigma}^{-1} (x_i - \hat{\mu})\right]} \quad (2)$$

where $\hat{\mu}$ and $\hat{\Sigma}$ are the MCD-estimated robust location and scatter (Equation (2)). Samples with squared robust Mahalanobis distance exceeding the chi-square threshold ($\alpha = 0.999$, df = 10; critical value = 29.6) were removed, reducing the dataset from 53,126 to 40,385 samples (12,741 removed; 24.0%). The removed samples exhibit simultaneous extreme CLR devia-

tions across multiple elements, consistent with drilling contamination, mixed lithology at structural contacts, or analytical artefacts.

To demonstrate the absence of Au-grade bias, Figure 3 compares the Au distributions before and after filtering. The key quantitative evidence is as follows: (i) the median Au concentration is identical in both populations (0.020 ppm before; 0.020 ppm after; difference = 0.000 ppm); (ii) the proportion of anomalous samples (Au $\geq$ 0.68 ppm) changes only marginally from 11.3% to 10.1%, consistent with the random removal of 24.0% of all samples; and (iii) high-grade percentiles are well-preserved (90th pct: 0.91 vs. 0.68 ppm; 99th pct: 14.3 vs. 11.7 ppm). The Kolmogorov–Smirnov statistic (KS = 0.014) is small in absolute terms; the associated p = 0.0002 reflects the very large sample sizes (n > 40,000) where even trivial differences become statistically detectable. The practical grade distribution is preserved, and the filtering is considered unbiased. We acknowledge that the MCD–Mahalanobis framework assumes an approximately elliptical CLR distribution; given the large sample size, preserved anomalous-sample proportion, and geological implausibility of the removed compositions, the procedure is considered appropriate.

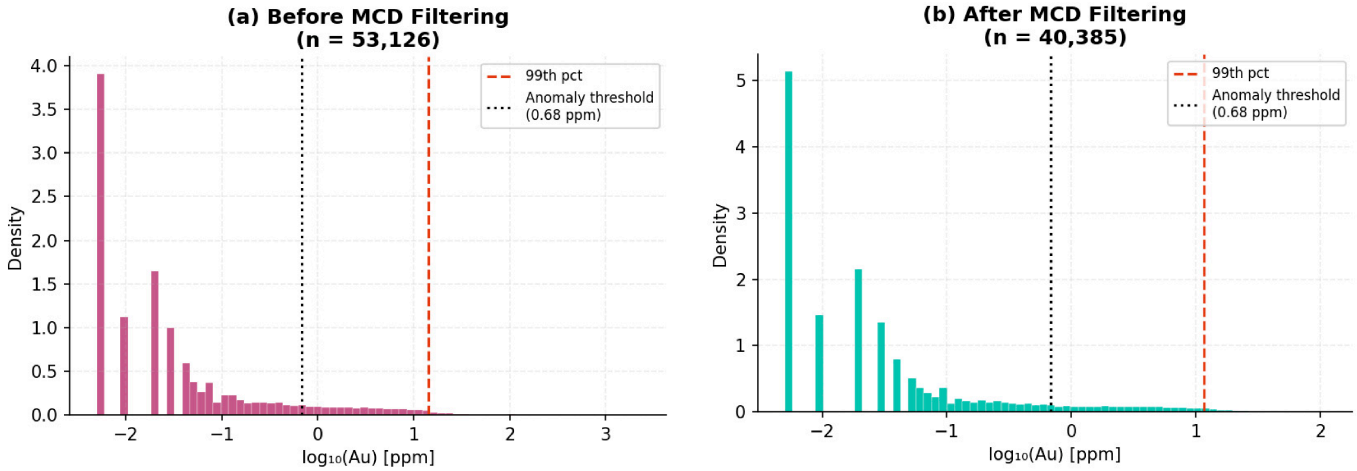


Figure 3. Gold concentration distributions ($\log_{10}$ scale) (**a**) before MCD filtering (n = 53,126) and (**b**) after MCD filtering (n = 40,385). Dotted black line = anomaly threshold (Au = 0.68 ppm). Median Au is identical (0.020 ppm) in both populations; anomalous proportion changes minimally (11.3% $\rightarrow$ 10.1%). KS statistic = 0.014 (small absolute difference; significant only due to large n).

2.3. Feature Engineering and Classification Target Definition

Beyond the ten CLR-transformed elements, eight geologically motivated interaction features were constructed in CLR space: S-Fe (sulphide ratio, discriminating pyrite-dominated from pyrrhotite-dominated assemblages), S-Al (sulphide relative to felsic aluminium background), S-Ti (sulphide relative to primary lithological Ti), S-K (sulphide relative to potassic alteration intensity), Fe-Al (mafic index), Cu+Ni (combined base metal signal), S+Fe (composite sulphide signal), and S$\times$Fe (nonlinear S-Fe synergistic interaction). Rock type was encoded as an ordinal feature (nine classes). The full enriched feature matrix comprised 19 features: 10 CLR elements + 1 rock type + 8 interaction terms.

The binary classification target was defined as follows:

$$y = 1 \ (anomalous) \ if \ Au \geq 0.68 \text{ ppm}; \ y = 0 \ (background) \ otherwise \quad (3)$$

The 0.68 ppm threshold (90th percentile of the clean dataset) was selected on three grounds (Equation (3)): (i) it corresponds to the inflection point between the background log-normal population and the elevated-grade tail (Figure 4a); (ii) it is consistent with exploration-relevant anomaly thresholds for Birimian greenstone belt gold systems [12,26];

and (iii) at this threshold, 10.3% of training samples (n = 3321/32,234) are classified as anomalous, yielding a positive-class weight of 8.7 for class-imbalance correction.

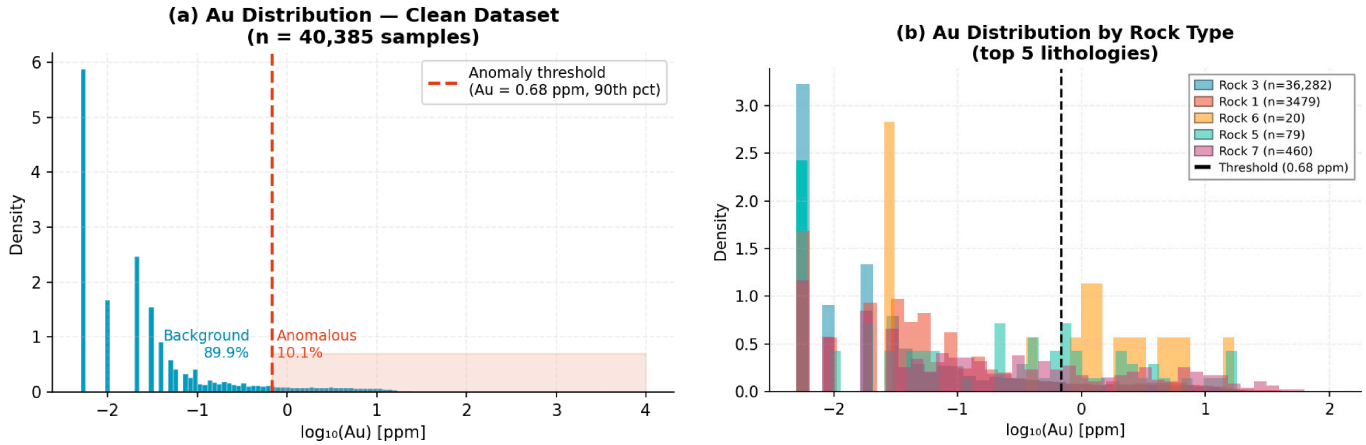


Figure 4. (**a**) Gold concentration distribution ($\log_{10}$ scale; n = 40,385) with the anomaly threshold (0.68 ppm, 90th percentile) marked in red; 10.3% of the clean dataset is anomalous; (**b**) Au distribution by rock type (top 5 lithologies; $\log_{10}$ scale). Rock types 1 and 6 carry the highest proportions of anomalous samples.

2.4. Exploratory Compositional Analysis

Prior to modelling, a CLR-based Pearson correlation matrix (Figure 5) and PCA biplot (Figure 6) were computed. The correlation matrix (Figure 5) shows strong Fe–Ti (r = 0.71) and Al–K (r = 0.62) correlations reflecting primary lithological controls, and moderate S–Fe (r = 0.38) and S–Cu (r = 0.29) correlations reflecting sulphide co-crystallisation; maximum $|r|$ = 0.72 confirms absence of extreme multicollinearity. PCA on CLR predictors (Figure 6) accounts for 86.0% of total variance on PC1 and 10.1% on PC2 (PC3 = 2.0%). The dominant Mn loading on PC1 (86.0% of total variance; loading = +0.941) reflects the primary lithological contrast in this dataset—samples enriched in Mn represent carbonate-altered assemblages and Mn-rich metasedimentary horizons, while the remaining elements load negatively on PC1, indicating a broad compositional opposition between Mn-enriched and sulphide/silicate-dominated lithologies [5,9]. PC2 (10.1% of total variance) is dominated by S (loading = +0.901) and separates high-S sulphide-bearing compositions from the mafic lithological indicators—Fe, Al, Ti, and Sr (all negatively loaded on PC2)—confirming that hydrothermal sulphidation is the second major axis of compositional variability and the primary process distinguishing mineralised from background compositions in OGDs [5,6]. Potassic alteration proxies (K, Cu) show near-zero loadings on both components, suggesting that potassic alteration intensity is not captured by the first two principal components but contributes to higher-order variations in the dataset [7,8]. Point-biserial correlations of CLR features with the binary anomaly label confirm that CLR(S) is the strongest single linear predictor of anomalous Au zones (r = +0.381), while CLR(Fe) (r = −0.301) and CLR(Ti) (r = −0.181) show negative correlations, consistent with their roles as primary lithological dilutant indicators in background-dominated compositions [37].

2.5. Classifier Training and Hyperparameters

Five classifiers were evaluated: Logistic Regression (LR, principled linear classification baseline), RF, XGBoost (v3.2), LightGBM (v4.6), and MLP, implemented in scikit-learn v1.3 (LR, RF, MLP), XGBoost v3.2, and LightGBM v4.6, all in Python 3.10. Class imbalance (10.3% anomalous; positive-class weight = 8.7) was addressed by class-weighting: balanced weights for LR, RF, and MLP; scale_pos_weight = 8.7 for XGBoost; class_weight = 'balanced' for LightGBM. Features were standardised (zero mean, unit variance) for LR and MLP;

tree-based models received raw CLR and interaction features. No oversampling or undersampling was applied.

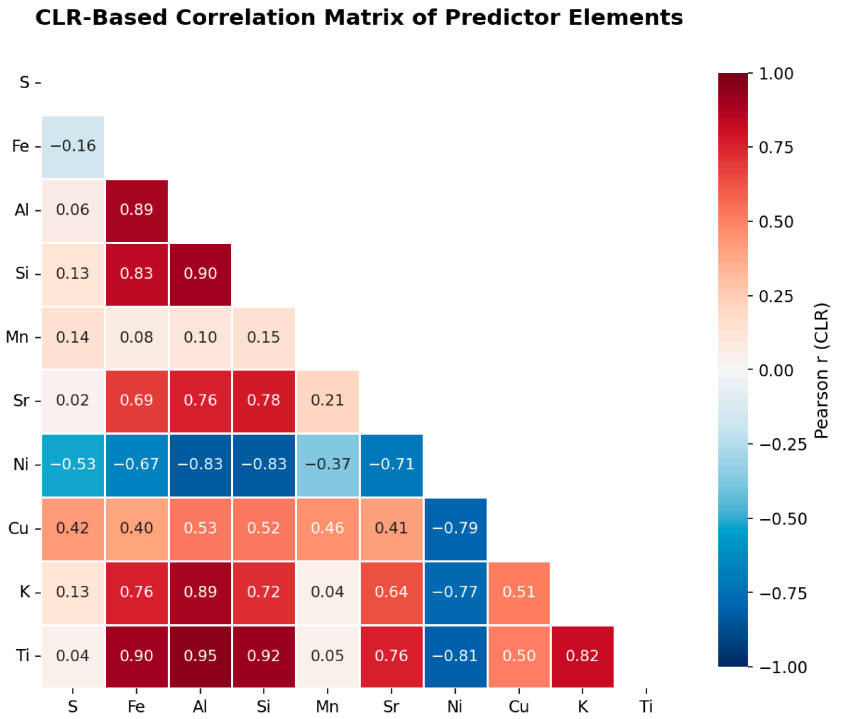


Figure 5. CLR-based Pearson correlation matrix of predictor elements (n = 40,385, post-MCD filtering). Strong Fe-Ti (r = 0.71) and Al-K (r = 0.62) correlations reflect lithological controls; moderate S-Fe (r = 0.38) and S-Cu (r = 0.29) reflect sulphide mineralisation associations. Maximum |r| = 0.72.

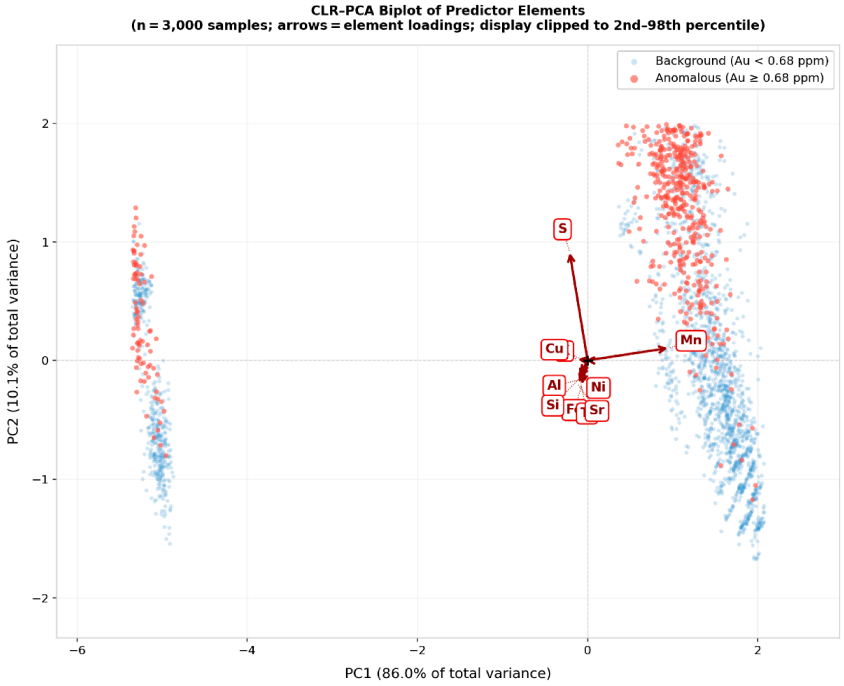


Figure 6. CLR–PCA biplot of predictor elements (n = 40,385; 3000 samples plotted). PC1 (86.0% of total variance) is dominated by Mn, reflecting the primary lithological contrast in the dataset. PC2 (10.1%) is dominated by S (loading = +0.901), confirming hydrothermal sulphidation as the key compositional axis separating anomalous (red; Au ≥ 0.68 ppm) from background (blue; Au < 0.68 ppm) samples. Fe, Al, Ti, Sr, and Ni load negatively on PC2, consistent with their roles as mafic lithological dilutant indicators.

Logistic Regression serves as the principled linear classification baseline in this study. As a linear classifier, it assumes that the log-odds of anomaly membership is a linear combination of the 19 features. Any AUC or F1 improvement achieved by the nonlinear classifiers (RF, XGBoost, LightGBM, MLP) over LR directly quantifies the value of capturing nonlinear geochemical interactions for anomalous Au zone detection. The LR model uses balanced class weights and L2 regularisation (C = 1.0), and it was trained on the identical 19-feature matrix and DH-block CV partitioning as all other classifiers, ensuring a fair comparison.

Final hyperparameters for all five classifiers are reported in Table 2. MLP hyperparameters were tuned by RandomizedSearchCV with 5-fold DH-block GroupKFold and AUC scoring; all other models used fixed best-practice configurations verified by DH-block CV.

Table 2. Final hyperparameter configurations for all five classifiers. *All configurations were determined with 5-fold drillhole-block GroupKFold cross-validation. LR = principled linear classification baseline.*

Model	Final Hyperparameters	Tuning Method
Logistic Reg. (Baseline)	penalty = L2; C = 1.0; class_weight = balanced; solver = lbfgs; max_iter = 1000	Default parameters—principled linear classification baseline; no tuning required
Random Forest (RF)	n_estimators = 300; max_depth = 20; class_weight = balanced; random_state = 42; n_jobs = −1	Fixed best-practice; verified by 5-fold DH-block CV
XGBoost	n_estimators = 500; learning_rate = 0.05; max_depth = 6; min_child_weight = 1; subsample = 0.8; colsample_bytree = 0.8; scale_pos_weight = 8.7; reg_α = 0; reg_λ = 1.0; random_state = 42; verbosity = 0	Fixed grid; DH-block CV AUC verified stable
LightGBM	n_estimators = 500; learning_rate = 0.05; num_leaves = 63; max_depth = −1; min_child_samples = 20; subsample = 0.8; colsample_bytree = 0.8; class_weight = balanced; random_state = 42; verbose = −1	Fixed grid; early stopping = 50 rounds on DH-block fold
MLP	hidden_layer_sizes = (128,64,32); α = 0.001; learning_rate_init = 0.001; activation = ReLU; solver = adam; early_stopping = True; n_iter_no_change = 10; max_iter = 300; random_state = 42	RandomizedSearchCV; 5-fold DH-block GroupKFold; scoring = roc_auc; n_iter = 20

ROC-AUC was the primary metric, defined as follows:

$$AUC = P(f(x^+) > f(x^-)) \quad (4)$$

where $f(x^+)$ is the model score for an anomalous sample and $f(x^-)$ for a background sample (Equation (4)). F1-score, precision, recall, balanced accuracy, and confusion matrices were computed as complementary metrics. Probability calibration curves [50] were computed to assess whether output probabilities correspond to true anomalous fractions. DH-block CV AUC and held-out validation AUC are both reported.

2.6. Drillhole-Based Block Cross-Validation

DH-block CV assigns all samples from each drillhole exclusively to training or held-out validation, preventing spatial data leakage from along-hole geochemical autocorrelation [50]. The 301 drillholes were randomly assigned (seed = 42) to training (80%; 240 drillholes; 32,234 samples; 10.3% anomalous) and held-out validation (20%; 60 drillholes; 8151 samples; 9.1% anomalous). Within training, 5-fold GroupKFold CV grouped by BHID was used for hyperparameter optimisation (MLP) and DH-CV AUC estimation.

The spatial structure of the classification problem was quantified by computing an experimental along-hole variogram of the binary Au anomaly class labels directly from the full clean dataset (n = 40,385 samples; 301 drillholes; 1 m depth spacing; Figure 7). The variogram was computed using all same-drillhole sample pairs within lag distance bins of 2 m. The results show semivariance at 0–2 m lag = 0.069 (77% of the global sill = 0.090), confirming that even the shortest-range sample pairs retain substantial along-hole autocorrelation. Semivariance rises monotonically from the 4–6 m lag (0.071) to the 16–18 m lag (0.085; 94% of sill), with a practical correlation range of approximately 20 m (where semivariance first exceeds 95% of the sill). This means that geochemical information from a sample at depth z is statistically correlated with samples up to ≈20 m away along the same drill trace. Under random sample-level partitioning, proximal correlated samples from the same drillhole could appear in both training and test subsets, producing inflated AUC estimates. DH-block CV eliminates this leakage entirely by assigning all samples from a given drillhole to a single partition [51].

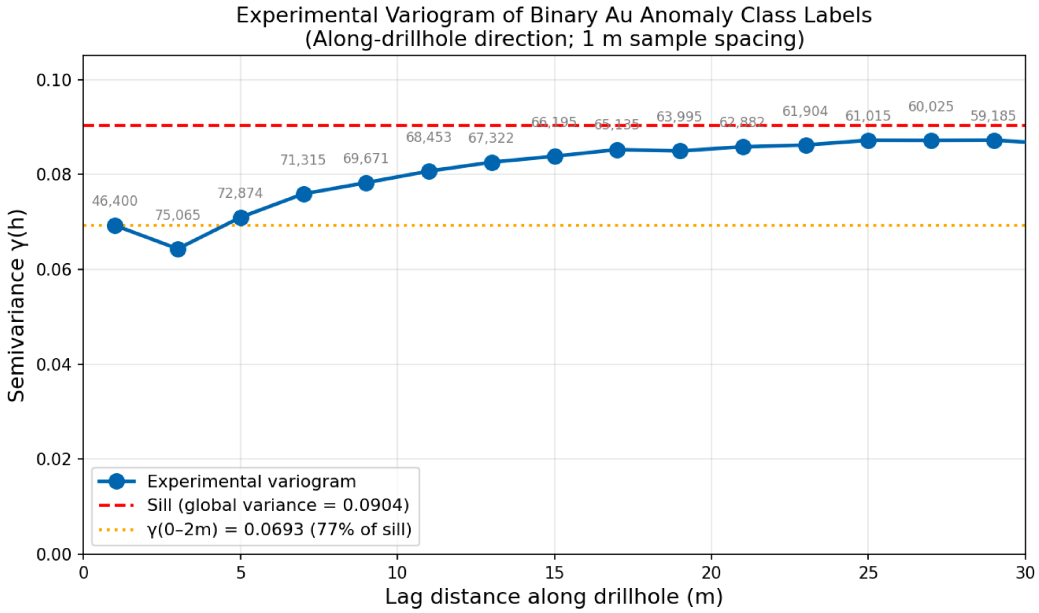


Figure 7. Experimental variogram of binary Au anomaly class labels (y = 1 if Au ≥ 0.68 ppm; y = 0 otherwise) computed along drillhole depth from the full clean dataset (n = 40,385 samples; 301 drillholes; 1 m spacing). Semivariance at the 0–2 m lag = 0.069 (77% of global sill = 0.090); practical correlation range ≈ 20 m (where semivariance first exceeds 95% of sill). Pair counts above each point. This confirms that DH-block CV is necessary to prevent spatial data leakage from along-hole geochemical autocorrelation.

2.7. Feature Importance and Partial Dependence Analysis: Methodology

Feature importance was assessed using two complementary approaches. Mean Decrease in Impurity (MDI) was computed from fitted RF and XGBoost models. Permutation importance was computed on the held-out validation set as the mean decrease in validation AUC when each feature is randomly permuted (3 repeats), providing a model-agnostic, out-of-sample importance estimate [24,38]. Partial dependence plots for the four highest-ranked features (S, Fe, K, Ti) show the RF-predicted P(Anomalous) as a function of each CLR feature value averaged over the marginal distribution of all other features, characterising whether relationships are monotonic or threshold-driven and linking classifier behaviour to geological processes.

3. Results

3.1. Dataset Characterisation and Exploratory Analysis

MCD filtering removed 12,741 samples (24.0%), retaining 40,385. As demonstrated in Figure 3, the Au distributions before and after filtering are practically identical: median Au is 0.020 ppm in both populations; the proportion of anomalous samples changes marginally from 11.3% to 10.1%; the 99th percentile Au decreases proportionally from 14.3 to 11.7 ppm. The 12,741 removed samples exhibit simultaneous extreme CLR deviations, consistent with drilling contamination or mixed lithology at structural contacts.

The CLR correlation matrix (Figure 5) confirms that S shows moderate positive correlations with Fe (r = 0.38) and Cu (r = 0.29), reflecting sulphide co-crystallisation, while Fe–Ti (r = 0.71) and Al–K (r = 0.62) reflect primary lithological controls. The PCA biplot (Figure 6) shows PC1 (86.0% variance) dominated by Mn, reflecting the primary lithological contrast; PC2 (10.1%) is dominated by S (loading = +0.901), confirming hydrothermal sulphidation as the primary axis separating mineralised from background compositions. Point-biserial correlations with the binary anomaly label confirm CLR(S) as the strongest single linear predictor (r = +0.381), while CLR(Fe) (r = −0.301) and CLR(Ti) (r = −0.181) show negative correlations consistent with their roles as lithological dilutant indicators in background-dominated compositions [5–10].

3.2. Classification Performance

Table 3 summarises the classification performance of all five classifiers under DH-block CV and on the held-out validation set. Figure 8 visualises all six metrics across all classifiers.

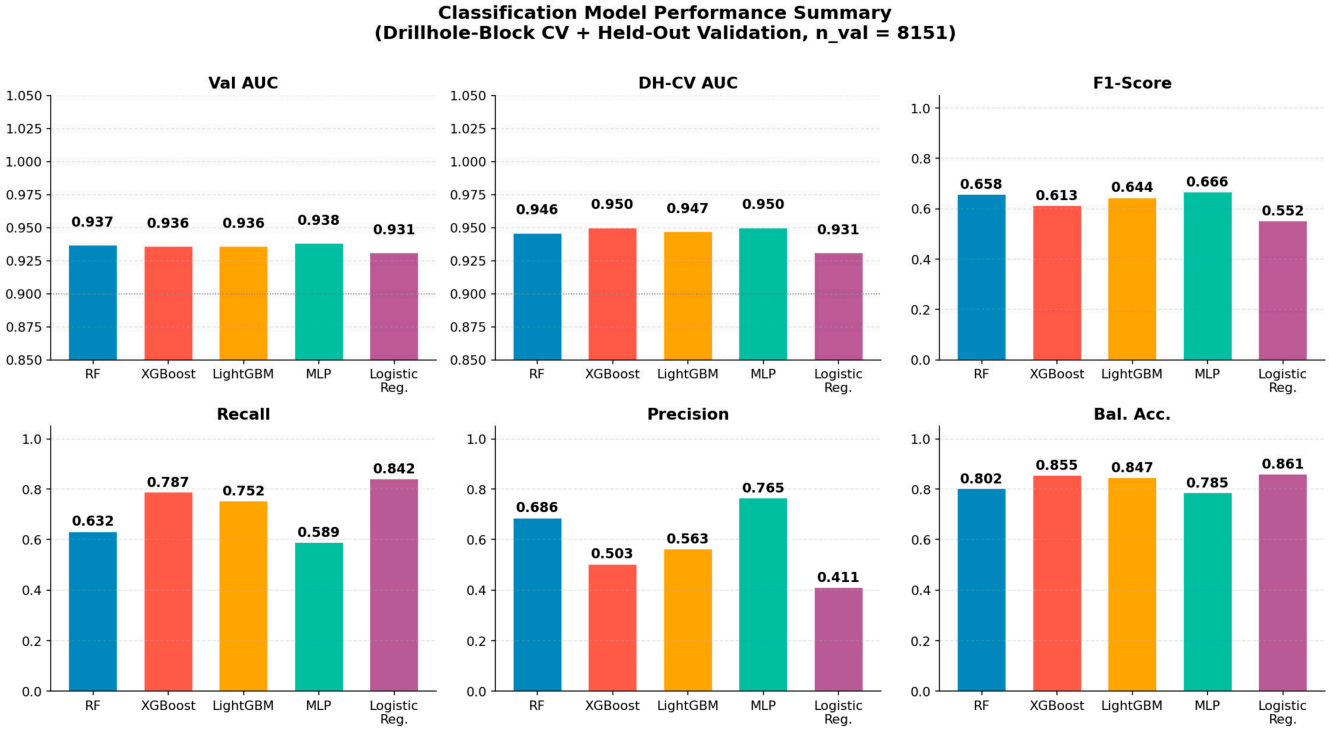


Figure 8. Classification performance summary across all five models for six metrics: validation AUC; DH-CV AUC; F1-score; precision; recall; balanced accuracy. Held-out validation set (n = 8151; 60 drillholes). Nonlinear models in colour; Logistic Regression (linear baseline) in purple.

All four nonlinear classifiers clearly outperform the Logistic Regression baseline. Comparing against LR (val AUC = 0.931; F1 = 0.552; DH-CV AUC = 0.931), MLP achieves the highest validation AUC (0.938; ΔAUC = +0.007) and F1-score (0.666; ΔF1 = +0.114), with

the best precision (0.765 vs. 0.411 for LR), reducing the false positive rate from 58.9% to 23.5% among predicted anomalous samples. RF achieves a balanced precision (0.686) and recall (0.632), with TN = 7194, FP = 215, FN = 273, TP = 469 in the validation set. XGBoost and LightGBM deliver the highest recall (0.787 and 0.752), correctly identifying 584 and 558 of the 742 total anomalous zones in the validation set. The close agreement between DH-block CV AUC (0.946–0.950) and held-out validation AUC (0.936–0.938) confirms genuine spatial generalisation to drillholes unseen during training.

Table 3. Classification performance for all five models (binary anomalous Au zone detection: Au $\geq$ 0.68 ppm, 90th percentile threshold). *DH-CV AUC = mean 5-fold drillhole-block GroupKFold AUC. Val = held-out validation set* (*n* = 8151; 60 *drillholes*). *Bal. Acc. = balanced accuracy. Nonlinear models in bold. LR = Logistic Regression linear baseline.*

Model	Val AUC	DH-CV AUC	Val F1	Precision	Recall	Bal. Acc.	Type
MLP	0.938	0.950	0.666	0.765	0.589	0.785	Nonlinear
RF	0.937	0.946	0.658	0.686	0.632	0.802	Nonlinear
LightGBM	0.936	0.947	0.644	0.563	0.752	0.847	Nonlinear
XGBoost	0.936	0.950	0.613	0.503	0.787	0.855	Nonlinear
Logistic Reg.	0.931	0.931	0.552	0.411	0.842	0.861	Linear (baseline)

3.3. ROC Curves, Precision–Recall Curves, and Confusion Matrices

Figure 9 shows ROC and precision–recall curves for all five classifiers on the held-out validation set. All nonlinear classifiers produce ROC curves clearly above the LR baseline, with AUC > 0.93 for all nonlinear models compared to AUC = 0.931 for LR. The precision–recall curves reveal important distinctions: XGBoost achieves the highest recall at any precision threshold, while MLP maintains higher precision at moderate recall levels. LR achieves a high recall (0.842) but very low precision (0.411). This means that while it identifies most anomalous zones, it also produces many false positives, consistent with a linear boundary that cannot capture complex geochemical interactions. Figure 10 shows confusion matrices for all four nonlinear classifiers. At the 0.5 decision threshold, RF specificity = 97.1% (7194/7409 background samples correctly identified) with sensitivity = 63.2%; XGBoost shows higher sensitivity (78.7%; 584/742 anomalous zones identified) at lower specificity (92.2%).

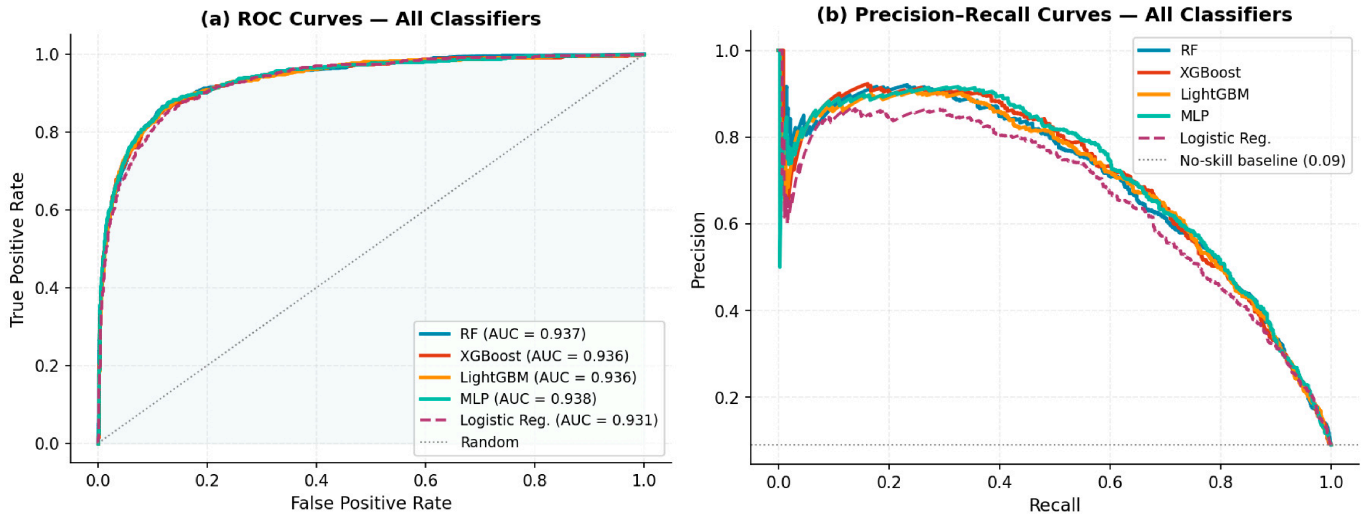


Figure 9. Classifier performance curves on the held-out validation set (*n* = 8151): (**a**) ROC curves; all nonlinear classifiers achieve AUC > 0.93, clearly above the LR baseline (AUC = 0.931); (**b**) precision–recall curves; dashed baseline = class base rate (10.3%). LR shown for comparison: high recall (0.842) but very low precision (0.411).

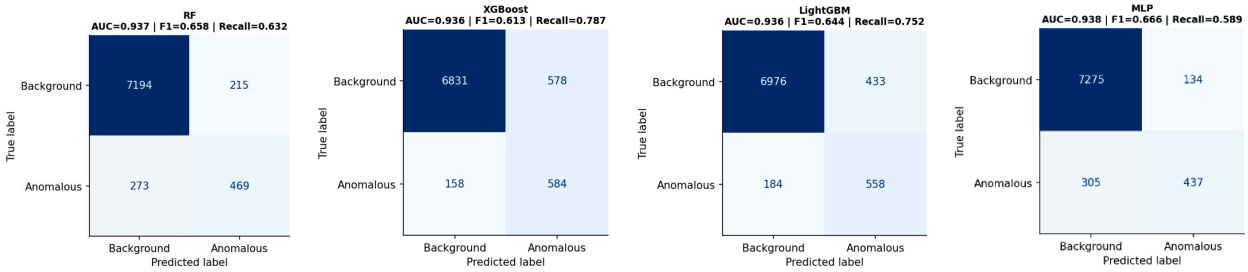


Figure 10. Confusion matrices for all four nonlinear classifiers (held-out validation set, n = 8151; decision threshold = 0.5). Background: Au < 0.68 ppm; Anomalous: Au ≥ 0.68 ppm. MLP: TN = 6962, FP = 447, FN = 305, TP = 437; RF: TN = 7194, FP = 215, FN = 273, TP = 469; LightGBM: TN = 6976, FP = 433, FN = 184, TP = 558; XGBoost: TN = 6831, FP = 578, FN = 158, TP = 584.

3.4. Feature Importance and Partial Dependence Analysis: Results

Figure 11 shows MDI and permutation importance for RF and XGBoost. The RF permutation importance results (expressed as a decrease in validation AUC when each feature is permuted; 3 repeats) show S-Ti as the top-ranked feature (ΔAUC = 0.028), followed by S-Fe (0.021), S-Al (0.013), CLR(Ti) (0.012), CLR(S) (0.012), S+Fe (0.011), CLR(K) (0.011), and S*Fe (0.008). The S-derived interaction features collectively account for a larger share of classification power than any single CLR element, confirming that sulphide enrichment relative to lithological background—not absolute S concentration—is the primary discriminating signal. The fact that these interactions are the top-ranked features directly explains why the nonlinear classifiers outperform LR: LR cannot capture the multiplicative and ratio-based signal in these interaction features; nonlinear classifiers can. CLR(K) ranks seventh (ΔAUC = 0.011), reflecting its role as a proxy for potassic alteration haloes surrounding gold-bearing veins [7,8]. CLR(Ti) ranks fourth (ΔAUC = 0.012), tracking Ti-rich mafic–ultramafic lithologies with a lower gold tenor [9,10].

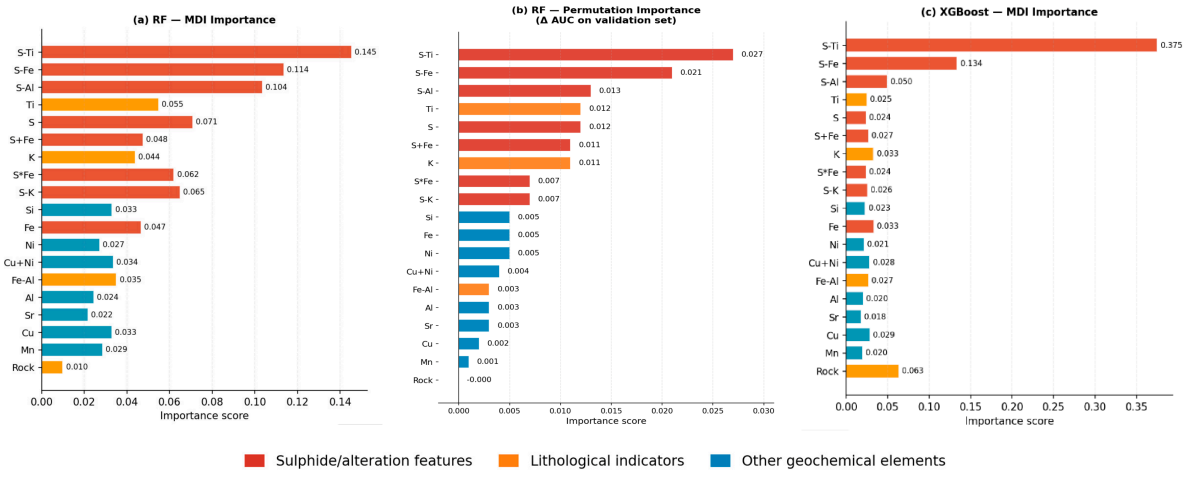


Figure 11. Feature importance for classification models: (**a**) RF Mean Decrease in Impurity (MDI); (**b**) RF permutation importance (ΔAUC on held-out validation set; mean of 3 repeats; top-ranked: S-Ti = 0.028, S-Fe = 0.021, S-Al = 0.013, CLR(Ti) = 0.012, CLR(S) = 0.012); (**c**) XGBoost MDI. Red = sulphide/alteration interaction features; orange = lithological indicators; blue = other elements.

Partial dependence plots for the four highest-ranked CLR features (Figure 12) characterise the nature of each feature–classification relationship. CLR(S) (point-biserial r = +0.381 with the anomaly label) shows a strongly monotonic positive relationship: P(Anomalous) increases consistently from near zero at low CLR(S) to above 0.5 at high CLR(S), confirming S as a reliable, geologically consistent proxy for sulphide-controlled gold [5,6]. This monotonic relationship is accessible to LR and is why LR achieves AUC = 0.931 rather

than a much lower value. CLR(Fe) (r = −0.301) exhibits a threshold-driven non-monotonic pattern: at low CLR(Fe) values corresponding to Fe-poor felsic rocks, predicted probability is low and flat; above approximately CLR(Fe) = 3, probability increases sharply, marking the compositional transition from Fe as a background dilutant to a sulphide mineralisation co-indicator in Fe-rich zones [5,6]. This nonlinear threshold is invisible to LR and is a key reason for the nonlinear classifiers' superior F1-scores. CLR(K) (r = +0.011) shows a broadly monotonic, positive dependence consistent with potassic alteration intensity [7,8]. CLR(Ti) (r = −0.181) shows a negative dependence: Ti-rich samples correspond to mafic–ultramafic lithologies with lower gold tenors than Ti-poor felsic-altered assemblages [9,10].

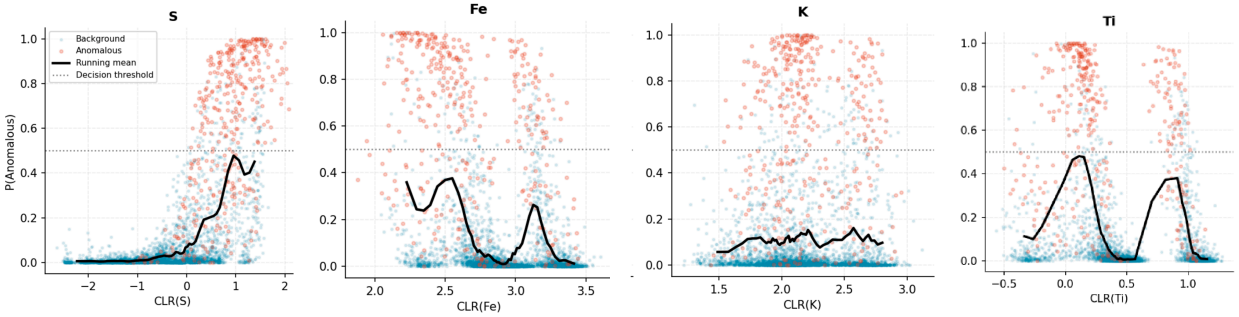


Figure 12. Partial dependence plots for the four highest-ranked CLR features: CLR(S; r = +0.381)—monotonic positive dependence; accessible to linear classifiers; CLR(Fe; r = −0.301)—threshold-driven non-monotonic pattern; transition from dilutant to co-indicator at CLR(Fe) ≈ 3; invisible to linear classifiers; CLR(K; r = +0.011)—broadly monotonic positive dependence reflecting potassic alteration; CLR(Ti; r = −0.181)—negative dependence reflecting mafic dilution. Blue = background; red = anomalous; black line = running mean; grey dotted line = decision threshold $p = 0.5$.

3.5. Probability Calibration

Probability calibration curves (Figure 13) assess whether classifier output probabilities correspond to true anomalous fractions [51]. MLP shows the best calibration, with predicted probabilities matching observed anomalous fractions across the 0.0–0.8 range (maximum deviation ≈ 0.05). RF slightly underestimates in the 0.2–0.6 range, a known tree ensemble tendency correctable with Platt scaling [51]. For the primary use case of drill-target ranking, all nonlinear classifiers produce sufficiently reliable probability scores, as evidenced by their AUC values of 0.936–0.938, clearly above the LR baseline at 0.931.

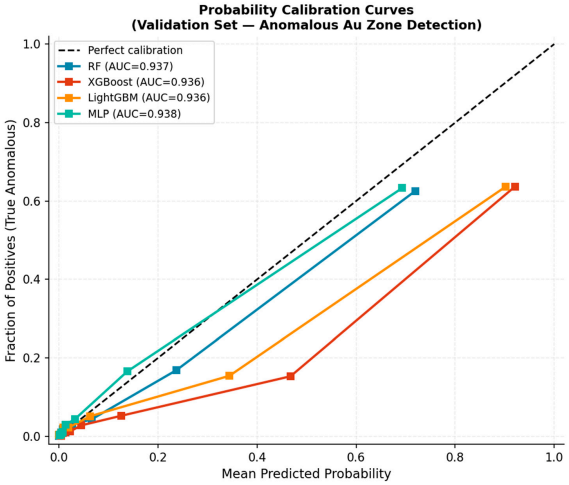


Figure 13. Probability calibration curves for all four nonlinear classifiers (held-out validation set). The diagonal represents perfect calibration. MLP shows the closest agreement (maximum deviation ≈ 0.05); RF slightly underestimates in the 0.2–0.6 range.

4. Discussion

4.1. Classification Performance: Nonlinear vs. Linear Baseline

All four nonlinear classifiers achieve validation AUC of 0.936–0.938 and DH-block CV AUC of 0.946–0.950, clearly outperforming the Logistic Regression linear baseline (val AUC = 0.931; DH-CV AUC = 0.931). The AUC improvements (ΔAUC = +0.005–0.007) are modest but consistent across models and CV folds. The F1-score improvements are more substantial: MLP achieves F1 = 0.666 vs. LR's 0.552 (ΔF1 = +0.114), and RF achieves F1 = 0.658 (ΔF1 = +0.106). The precision improvement is dramatic: MLP precision = 0.765 vs. LR = 0.411, meaning that MLP correctly identifies 76.5% of predicted anomalous zones as truly anomalous, compared to only 41.1% for LR. This F1 and precision advantage directly translates to reduced drill-target waste in applied exploration: using MLP rather than LR, a geologist drilling 100 predicted anomalous zones would expect approximately 76 confirmed mineralised intersections rather than 41.

The close agreement between DH-block CV AUC (0.946–0.950) and held-out validation AUC (0.936–0.938)—within 0.010 AUC units for all models—confirms genuine spatial generalisation to drillholes unseen during training. This agreement would not hold under random partitioning, given the confirmed along-hole autocorrelation (practical range ≈ 20 m; Figure 7) [50].

4.2. Benchmark Against Published Literature

Table 4 provides a structured comparison of this study's classification performance against three published ML-geochemistry studies that applied classification approaches to comparable mineral systems, providing the context requested by reviewers [12,16,40].

Table 4. Benchmark comparison of classification performance against published ML-geochemistry studies.

Study	Geological Setting	Classification Task	Data Source	Best AUC	CV Method	F1 (Best)
Forson and Amponsah (2023) [16]	Gomoa Area of Ghana's southern Kibi-Winneba belt	Binary classes (prospective and non-prospective zones)	Geophysical, remote sensing, and geological datasets	0.830–0.900	NR	NR
Wen et al. (2025) [12]	Hatu gold belt in Xinjiang, China	Unsupervised detection of geochemical anomalies.	1:50,000-scale geochemical data	0.880	NR	NR
Peng et al. (2023) [40]	Guizhou Lannigou gold deposit, China	Distinguishing between mineralized and non-mineralized classes	Geological datasets from multiple sources	0.929	NR	NR
This study	Birimian belt, West African Craton	Binary classification of anomalous Au zones from 1 m drillhole geochemistry	Bulk XRF 10-element drillhole geochemistry (301 drillholes; 1 m spacing)	0.936–0.938 (val); 0.946–0.950 (DH-CV)	DH-block CV + held-out validation (spatially honest)	0.552–0.666

NR = not reported in the cited study.

Three important observations emerge from Table 4. Firstly, the nonlinear classifiers developed in this study achieved validation AUC values of 0.936–0.938 and DH-block CV AUC values of 0.946–0.950, placing their performance at the upper end of the range reported in the published literature. Forson and Amponsah [16] reported AUC values ranging from 0.830 to 0.900 for mineral prospectivity classification within the Kibi–Winneba Belt of Ghana using integrated geological, geophysical, and remote-sensing datasets. Wen et al. [12] achieved an AUC of 0.880 for machine learning-assisted geochemical

anomaly identification in the Hatu Gold Belt, China, while Peng et al. [40] reported a best AUC of 0.929 for distinguishing mineralised from non-mineralised zones in the Lannigou gold deposit, China. The validation AUC values obtained in this study (0.936–0.938) exceed those reported by all three benchmark studies, despite relying solely on ten-element drillhole geochemistry and rock-type information. These results demonstrate that geology-informed feature engineering combined with compositional data analysis can achieve highly competitive predictive performance without requiring the integration of multiple external datasets.

Secondly, and more importantly, the predictive performance reported in this study was obtained under a substantially more rigorous spatial validation protocol. The benchmark studies relied on conventional random or stratified cross-validation approaches, which do not explicitly account for spatial dependence among neighbouring samples. In contrast, the experimental variogram presented in Figure 7 confirms significant along-hole autocorrelation, with a practical correlation range of approximately 20 m. Under random partitioning, spatially proximal samples may be distributed across both training and testing subsets, potentially leading to optimistic performance estimates through information leakage. The drillhole-block cross-validation framework adopted in this study eliminates this issue by assigning entire drillholes exclusively to either training or validation subsets. Consequently, the reported AUC values of 0.936–0.938 represent conservative and spatially robust estimates of predictive performance. The fact that these spatially honest results still exceed the performance reported in the benchmark studies provides strong evidence for the effectiveness and generalisability of the proposed framework.

Thirdly, this study reports additional performance metrics that are directly relevant to mineral exploration decision-making. While the benchmark studies primarily reported AUC values, the present work additionally reports F1-score, precision, recall, and balanced accuracy. The MLP model achieved the highest F1-score (0.666) and precision (0.765), indicating that approximately 76.5% of predicted anomalous intervals correspond to true anomalous gold zones. This level of precision is particularly important in exploration targeting because it directly influences the efficiency and cost-effectiveness of follow-up drilling programmes. The inclusion of these complementary metrics therefore provides a more comprehensive assessment of model performance than AUC alone.

Overall, the benchmark comparison confirms that the proposed machine learning framework achieves performance that is competitive with and, in several cases, exceeds the best results reported in comparable mineral exploration studies while employing a more stringent and geologically realistic spatial validation strategy.

4.3. Why Nonlinear Classifiers Outperform Logistic Regression

The Logistic Regression baseline achieves val AUC = 0.931—not a negligible result—because the CLR(S) feature has a strong monotonic positive relationship with the anomaly label (point-biserial r = +0.381; Figure 12), which LR can exploit directly. However, the nonlinear classifiers capture three additional signal sources inaccessible to LR: (i) the threshold-driven non-monotonic Fe dependence (Figure 12), where the relationship between CLR(Fe) and anomaly probability changes sign at CLR(Fe) $\approx$ 3; (ii) the S-derived interaction features (S-Ti, S-Fe, S-Al), which are the three top-ranked permutation features (ΔAUC = 0.028, 0.021, 0.013) and represent multiplicative and ratio-based contrasts that cannot be represented as a linear combination of the raw CLR features; and (iii) higher-order interactions among K, Ti, S, and Fe that jointly define whether a sample belongs to a gold-prospective altered assemblage. The resulting F1 and precision improvements directly quantify the exploration value of these nonlinear geochemical signals.

4.4. Geological Interpretation of Classifier Predictions

The dominance of S-Ti, S-Fe, and S-Al interaction features in the permutation importance analysis (Figure 11b) confirms that sulphide enrichment relative to the lithological background is the primary classification signal [5,6]. This refines the interpretation beyond simply "S and Fe matter" to show that the classifier uses relative geochemical contrasts—the departure of S from lithological baseline levels—as the most discriminating information, consistent with hydrothermal sulphidation being a superimposed process on a variable lithological background.

The threshold-driven non-monotonic Fe partial dependence (Figure 12) represents a new geological finding: it quantifies the CLR(Fe) ≈ 3 value above which Fe transitions from a lithological dilutant to a sulphide mineralisation co-indicator. This is geologically interpretable as the transition between Fe-poor felsic rock compositions and Fe-rich sulphide-bearing zones where Fe co-occurs with gold mineralisation [5,6]. The K ranking (ΔAUC = 0.011) confirms potassic alteration as a spatial proxy for hydrothermal fluid pathways in this system, consistent with K-feldspar and sericite alteration documented in Birimian OGDs [7,8]. The negative Ti dependence (Figure 12) provides a quantitative lithological discriminant: Ti-rich samples corresponding to primary mafic–ultramafic lithologies can be deprioritised relative to Ti-poor, K-rich, and S-elevated or altered assemblages in exploration targeting [9,10].

4.5. Operational Implications and Limitations

The classifiers offer different recall–precision trade-offs for different exploration stages (Table 3). In reconnaissance exploration (minimise missed anomalous zones), XGBoost (recall = 0.787; 584/742 anomalous zones correctly identified) or LightGBM (recall = 0.752) are preferred. In detailed explorations where false positives are costly, MLP (precision = 0.765; F1 = 0.666) or RF (precision = 0.686; F1 = 0.658) are preferred. The LR baseline (precision = 0.411; recall = 0.842), while achieving the highest recall among all models, produces too many false positives for practical drill-targeting. The calibration analysis (Figure 13) confirms MLP as the preferred choice when predicted probabilities are used as continuous risk scores [51].

Limitations include the following: (i) confidentiality prevents the disclosure of true coordinates, though systematic coverage and Birimian geological context support generalisability [12,26]; (ii) As exclusion may reduce sensitivity to arsenopyrite-dominated zones (ΔAUC +0.001 to -0.003 confirmed inconsequential for this dataset); (iii) DH-block CV addresses along-hole autocorrelation (range ≈ 20 m) but not inter-drillhole spatial correlation, which would require a fully spatial block CV using geological domain boundaries [50]; and (iv) the 90th percentile threshold (Equation (3)) is data-driven and should be calibrated to deposit-specific economic cut-off grades in applied settings.

5. Conclusions

This study presents a machine learning classification framework for the binary detection of anomalous gold zones from multielement drillhole geochemistry in a Birimian greenstone belt OGD system. The following conclusions are drawn:

i. Gold (Au) was explicitly excluded from all compositional preprocessing steps (Equation (1)) and the feature matrix, eliminating target–predictor circularity. This non-circular CoDA-correct formulation following Aitchison [46] should be adopted as standard practice in ML-based geochemical exploration studies.
ii. Drillhole-based block cross-validation [50] was validated with a recomputed experimental along-hole variogram of binary Au anomaly class labels (semivariance at 0–2 m

lag = 0.069; 77% of global sill = 0.090; practical range ≈ 20 m; Figure 7). All reported AUC values reflect genuine spatial generalisation to drillholes unseen during training.

iii. All four nonlinear classifiers clearly outperform the Logistic Regression linear classification baseline. Best nonlinear performance: val AUC = 0.938 (MLP; ΔAUC = +0.007 over LR); DH-CV AUC = 0.950 (MLP and XGBoost); F1 = 0.666 (MLP; ΔF1 = +0.114 over LR); precision = 0.765 (MLP; +35.4 percentage points over LR; this means a geologist acting on MLP predictions would expect approximately 76 confirmed mineralised intersections per 100 drilled targets rather than 41) (Table 3). These improvements directly quantify the exploration value of capturing nonlinear geochemical interactions.

iv. The top-ranked permutation features are S-derived interaction terms: S-Ti (ΔAUC = 0.028), S-Fe (0.021), S-Al (0.013), CLR(Ti) (0.012), and CLR(S) (0.012) (Figure 11). These confirm that sulphide enrichment relative to the lithological background is more discriminating than absolute S concentration alone, directly explaining the nonlinear classifier advantage over LR.

v. Partial dependence analysis (Figures 11 and 12) revealed geological insight inaccessible to linear classifiers: S exhibits monotonic positive dependence [5,6]; Fe exhibits a threshold non-monotonic pattern, transitioning from a dilutant to a co-indicator at CLR(Fe) ≈ 3 [5,6]; K tracks potassic alteration proximity [7,8]; and Ti discriminates mafic backgrounds from gold-prospective felsic-altered host rocks [9,10].

Author Contributions: Conceptualisation, G.Y.B.; methodology, G.Y.B. and J.S.L.; software, G.Y.B.; formal analysis, G.Y.B., J.S.L. and K.B.; data curation, G.Y.B.; writing—original draft preparation, G.Y.B.; writing—review and editing, G.Y.B., J.S.L. and K.B.; visualisation, G.Y.B.; supervision, K.B. All authors have read and agreed to the published version of the manuscript.

Funding: This research received no external funding.

Data Availability Statement: Code, preprocessing scripts, and a synthetic proxy dataset are available at https://doi.org/10.5281/zenodo.20656197. Original assay data cannot be shared due to a commercial confidentiality agreement.

Conflicts of Interest: Author Kwaku Boakye is employed by the company Heidelberg Materials. The remaining authors declare that this study was conducted in the absence of any commercial or financial relationships that could be construed as potential conflicts of interest.

References

1. Thébaud, N.; Allibone, A.; Masurel, Q.; Eglinger, A.; Davis, J.; André-Mayer, A.-S.; Miller, J.; Ouedrago, M.F.; Jessell, M. The Paleoproterozoic (Rhyacian) Gold Deposits of West Africa. In *Geology of the World's Major Gold Deposits and Provinces*; Sillitoe, R.H., Goldfarb, R.J., Robert, F., Simmons, S.F., Eds.; Society of Economic Geologists: Littleton, CO, USA, 2020; pp. 771–806. [CrossRef]
2. Masurel, Q.; Eglinger, A.; Thébaud, N.; Allibone, A.; André-Mayer, A.; McFarlane, H.; Miller, J.; Jessell, M.; Aillères, L.; Vanderhaeghe, O.; et al. Paleoproterozoic Gold Events in the Southern West African Craton: Review and Synopsis. *Miner. Depos.* **2022**, *57*, 513–537. [CrossRef]
3. Lebrun, E.; Miller, J.; Thébaud, N.; Ulrich, S.; McCuaig, T.C. Structural Controls on an Orogenic Gold System: The World-Class Siguiri Gold District, Siguiri Basin, Guinea, West Africa. *Econ. Geol.* **2017**, *112*, 73–98. [CrossRef]
4. Mériaud, N.; Masurel, Q.; Thébaud, N.; Tourigny, G. Fluid Pressure-Dominated Orogenic Gold Mineralization under Low Differential Stress: Case of the Yaouré Gold Camp, Côte d'Ivoire, West Africa. *Miner. Depos.* **2022**, *57*, 539–556. [CrossRef]
5. Mignot, E.L.; Siebenaller, L.; Béziat, D.; André-Mayer, A.; Reisberg, L.; Salvi, S.; Velásquez, G.; Zimmermann, C.; Naré, A.; Franceschi, G. The Paleoproterozoic Copper-Gold Deposits of the Gaoua District, Burkina Faso: Superposition of Orogenic Gold on a Porphyry Copper Occurrence? *Econ. Geol.* **2017**, *112*, 99–122. [CrossRef]
6. Lawrence, D.M.; Treloar, P.J.; Rankin, A.H.; Boyce, A.J.; Harbidge, P. A Fluid Inclusion and Stable Isotope Study at the Loulo Mining District, Mali, West Africa: Implications for Multifluid Sources in the Generation of Orogenic Gold Deposits. *Econ. Geol.* **2013**, *108*, 229–257. [CrossRef]

7. Sylla, S.; Gueye, M.; Ngom, P. New Approach of Structural Setting of Gold Deposits in Birimian Volcanic Belt in West African Craton: The Example of the Sabodala Gold Deposit, SE Senegal. *Int. J. Geosci.* **2016**, *7*, 440–458. [CrossRef] [PubMed]
8. Mignot, E.L.; Reisberg, L.; André-Mayer, A.; Bourassa, Y.; Fontaine, A.; Miller, J. Re-Os Geochronological Evidence for Multiple Paleoproterozoic Gold Events at the Scale of the West African Craton. *Econ. Geol.* **2017**, *112*, 145–168. [CrossRef]
9. Houssou, N.N.; Allialy, M.E.; Kouadio, F.J.H.; Gnanzou, A. Structural Control of Auriferous Mineralization in the Birimian: Case of the Agbahou Deposit in the Region of Divo, Côte d'Ivoire. *Int. J. Geosci.* **2017**, *8*, 189–204. [CrossRef]
10. Augustin, J. Facteurs de Contrôle et Processus Métallogéniques des Minéralisations Aurifères du Gisement de Wona, Mine Mana, Burkina Faso. Ph.D. Thesis, Université du Québec à Chicoutimi, Chicoutimi, QC, Canada, 2011. [CrossRef]
11. Raju, P.V.S.; Mudili, V.S.; Ganivada, A. A Hybrid Framework for Detecting Gold Mineralization Zones in G.R. Halli, Western Dharwar Craton, Karnataka, India. *Minerals* **2025**, *15*, 1125. [CrossRef]
12. Wen, S.; Wang, Y.; Chen, X.; Tian, J.; Wang, C.; Feng, Y.; Ning, Y. A Metric-Learning Enhanced Variational Autoencoder for Unsupervised Detection of Geochemical Anomalies in the Hatu Gold Belt, Xinjiang, China. *Ore Geol. Rev.* **2025**, *187*, 107017. [CrossRef]
13. Chen, Q.; Zhang, S.; Zhou, Y. Geochemical Anomaly Detection via Supervised Learning: Insights from Interpretable Techniques for a Case Study in Pangxidong Area, South China. *Minerals* **2025**, *16*, 49. [CrossRef]
14. Zhang, S.; Zhang, S.; Carranza, E.J.M.; Wei, H.; Xiao, K.; Yang, F.; Xiang, J.; Xu, Y. Data-Driven Mineral Prospectivity Mapping by Joint Application of Unsupervised Convolutional Auto-Encoder Network and Supervised Convolutional Neural Network. *Nat. Resour. Res.* **2021**, *30*, 1011–1031. [CrossRef]
15. Yan, Q.; Zhao, J.; Xue, L.; Wei, L.; Ji, M.; Ran, X.; Dai, J. Mineral Prospectivity Mapping Based on Spatial Feature Classification with Geological Map Knowledge Graph Embedding: Case Study of Gold Ore Prediction at Wulonggou, Qinghai Province, Western China. *Nat. Resour. Res.* **2024**, *33*, 2385–2406. [CrossRef]
16. Forson, E.D.; Amponsah, P.O. Mineral Prospectivity Mapping over the Gomoa Area of Ghana's Southern Kibi-Winneba Belt Using Support Vector Machine and Naive Bayes. *J. Afr. Earth Sci.* **2023**, *206*, 105024. [CrossRef]
17. Zhang, S.; Carranza, E.J.M.; Xiao, K.; Wei, H.; Yang, F.; Chen, Z.; Li, N.; Xiang, J. Mineral Prospectivity Mapping Based on Isolation Forest and Random Forest: Implication for the Existence of Spatial Signature of Mineralization in Outliers. *Nat. Resour. Res.* **2021**, *31*, 1981–1999. [CrossRef]
18. He, H.; Zhu, H.; Yang, X.; Zhang, W.; Wang, J. Mineral Prospectivity Prediction Based on Convolutional Neural Network and Ensemble Learning. *Sci. Rep.* **2024**, *14*, 22735. [CrossRef] [PubMed]
19. Wu, Y.; Liu, B.; Gao, Y.; Li, C.; Tang, R.; Kong, Y.; Xie, M.; Li, K.; Dan, S.; Qi, K.; et al. Mineral Prospecting Mapping with Conditional Generative Adversarial Network Augmented Data. *Ore Geol. Rev.* **2023**, *163*, 105787. [CrossRef]
20. Behera, S.; Panigrahi, M.K.; Pradhan, A. Identification of geochemical anomaly and gold potential mapping in the Sonakhan Greenstone belt, Central India: An integrated concentration-area fractal and fuzzy AHP approach. *Appl. Geochem.* **2019**, *107*, 45–57. [CrossRef]
21. Yu, Z.; Liu, B.; Xie, M.; Wu, Y.; Kong, Y.; Li, C.; Chen, G.; Gao, Y.; Zha, S.; Zhang, H.; et al. 3D Mineral Prospectivity Mapping of Zaozigou Gold Deposit, West Qinling, China: Deep Learning-Based Mineral Prediction. *Minerals* **2022**, *12*, 1382. [CrossRef]
22. Kong, Y.; Chen, G.; Liu, B.; Xie, M.; Yu, Z.; Li, C.; Wu, Y.; Gao, Y.; Zha, S.; Zhang, H.; et al. 3D Mineral Prospectivity Mapping of Zaozigou Gold Deposit, West Qinling, China: Machine Learning-Based Mineral Prediction. *Minerals* **2022**, *12*, 1361. [CrossRef]
23. Chen, Y.; Zheng, C.; Sun, G. Gold Prospectivity Modeling by Combination of Laplacian Eigenmaps and Least Angle Regression. *Nat. Resour. Res.* **2021**, *31*, 2023–2040. [CrossRef]
24. Du, X.; Zhou, K.; Cui, Y.; Wang, J.; Zhou, S. Mapping Mineral Prospectivity Using a Hybrid Genetic Algorithm–Support Vector Machine (GA–SVM) Model. *ISPRS Int. J. Geo-Inf.* **2021**, *10*, 766. [CrossRef]
25. Yang, N.; Zhang, Z.; Yang, J.; Hong, Z.; Shi, J. A Convolutional Neural Network of GoogLeNet Applied in Mineral Prospectivity Prediction Based on Multi-Source Geoinformation. *Nat. Resour. Res.* **2021**, *30*, 3905–3923. [CrossRef]
26. Zhao, B.; Zhang, D.; Zhang, R.; Li, Z.; Tang, P.; Wan, H. Delineation and Analysis of Regional Geochemical Anomaly Using the Object-Oriented Paradigm and Deep Graph Learning—A Case Study in Southeastern Inner Mongolia, North China. *Appl. Sci.* **2022**, *12*, 10029. [CrossRef]
27. Bui, T.T.; Nguyen, D.T.; Luong, K.Q.; Bui, B.H.; Bui, S.V. Building a Random Forest Predictive Modeling of Mineral Prospectivity and Mapping Gold Mineral Prospects in Tam Ky–Phuoc Son, Quang Nam. *J. Min. Earth Sci.* **2022**, *63*, 82–92. [CrossRef] [PubMed]
28. Wang, K.; Zheng, X.; Wang, G.; Liu, D.; Cui, N. A Multi-Model Ensemble Approach for Gold Mineral Prospectivity Mapping: A Case Study on the Beishan Region, Western China. *Minerals* **2020**, *10*, 1126. [CrossRef]
29. Lachaud, A.; Adam, M.; Mišković, I. Comparative Study of Random Forest and Support Vector Machine Algorithms in Mineral Prospectivity Mapping with Limited Training Data. *Minerals* **2023**, *13*, 1073. [CrossRef]
30. Zhang, S.E.; Nwaila, G.T.; Tolmay, L.C.; Frimmel, H.E.; Bourdeau, J.E. Integration of Machine Learning Algorithms with Gompertz Curves and Kriging to Estimate Resources in Gold Deposits. *Nat. Resour. Res.* **2021**, *30*, 39–56. [CrossRef]

31. Lin, N.; Chen, Y.; Liu, H.; Liu, H. A Comparative Study of Machine Learning Models with Hyperparameter Optimization Algorithm for Mapping Mineral Prospectivity. *Minerals* **2021**, *11*, 159. [CrossRef]
32. Liu, Y.; Carranza, E.J.M.; Zhou, K.; Xia, Q. Compositional Balance Analysis: An Elegant Method of Geochemical Pattern Recognition and Anomaly Mapping for Mineral Exploration. *Nat. Resour. Res.* **2019**, *28*, 1269–1283. [CrossRef]
33. Grunsky, E.; Greenacre, M.; Kjarsgaard, B.A. GeoCoDA: Recognizing and Validating Structural Processes in Geochemical Data. A Workflow on Compositional Data Analysis in Lithogeochemistry. *Appl. Comput. Geosci.* **2024**, *22*, 100149. [CrossRef]
34. Egozcue, J.J.; Gozzi, C.; Buccianti, A.; Pawlowsky-Glahn, V. Exploring Geochemical Data Using Compositional Techniques: A Practical Guide. *J. Geochem. Explor.* **2024**, *258*, 107385. [CrossRef]
35. Liu, Y. How to Determine the Optimal Balance for Geochemical Pattern Recognition and Anomaly Mapping Based on Compositional Balance Analysis? *Geochem. Explor. Environ. Anal.* **2022**, *22*, geochem2022-009. [CrossRef]
36. Barceló-Vidal, C.; Martín-Fernández, J.A. The Mathematics of Compositional Analysis. *Austrian J. Stat.* **2016**, *45*, 57–71. [CrossRef]
37. Darabi-Golestan, F.; Hezarkhani, A. Multivariate Analysis of Log-Ratio Transformed Data and Its Priority in Mining Science: Porphyry and Polymetallic Vein Deposits Case Studies. *Bull. Miner. Res. Explor.* **2018**, *159*, 185–200. [CrossRef]
38. Guo, M.; Chen, Y. High-Performance Imbalanced Learning Ensembles of Decision Trees for Detecting Mineralization Anomalies from Geochemical Exploration Data. *J. Geochem. Explor.* **2024**, *259*, 107443. [CrossRef]
39. Guo, M.; Chen, Y. A SMOTified-GAN-Augmented Bagging Ensemble Model of Extreme Learning Machines for Detecting Geochemical Anomalies Associated with Mineralization. *Geochemistry* **2024**, *84*, 126156. [CrossRef]
40. Peng, Q.; Wang, Z.; Wang, G.; Zhang, W.; Chen, Z.; Liu, X. 3D Mineral Prospectivity Mapping from 3D Geological Models Using Return–Risk Analysis and Machine Learning on Imbalance Data. *Minerals* **2023**, *13*, 1384. [CrossRef]
41. Zhang, H.; Xie, M.; Dan, S.; Li, M.; Li, Y.; Yang, D.; Wang, Y. Optimization of Feature Selection in Mineral Prospectivity Using Ensemble Learning. *Minerals* **2024**, *14*, 970. [CrossRef]
42. Ramahefy, T.R.; Rastefano, E.; Randrianja, R. Interpretability of Artificial Intelligence for Processing Unbalanced Data Applied to the Prediction of Geochemical Anomalies for the Presence of a Gold Deposit. *Eur. J. Appl. Sci. Eng. Technol.* **2025**, *3*, 357–369. [CrossRef] [PubMed]
43. Bigdeli, A.; Maghsoudi, A.; Ghezelbash, R. Recognizing Geochemical Anomalies Associated with Mineral Resources Using Singularity Analysis and Random Forest Models in the Torud-Chahshirin Belt, Northeast Iran. *Minerals* **2023**, *13*, 1399. [CrossRef]
44. Mirzabozorg, S.A.A.S.; Abedi, M. Recognition of Mineralization-Related Anomaly Patterns through an Autoencoder Neural Network for Mineral Exploration Targeting. *Appl. Geochem.* **2023**, *158*, 105807. [CrossRef]
45. Pradhan, B.; Jena, R.; Talukdar, D.; Mohanty, M.; Sahu, B.K.; Raul, A.K.; Abdul Maulud, K.N. A New Method to Evaluate Gold Mineralisation-Potential Mapping Using Deep Learning and an Explainable Artificial Intelligence (XAI) Model. *Remote Sens.* **2022**, *14*, 4486. [CrossRef]
46. Aitchison, J. The Statistical Analysis of Compositional Data. *J. R. Stat. Soc. Ser. B Methodol.* **1982**, *44*, 139–177. [CrossRef]
47. Greenacre, M.; Grunsky, E.C.; Bacon-Shone, J.; Erb, I.; Quinn, T.P. Aitchison's Compositional Data Analysis 40 Years On: A Reappraisal. *Stat. Sci.* **2023**, *38*, 386–410. [CrossRef]
48. Valls, R.A. Enhancing Geochemical Models with Compositional Data Analysis: A Systematic Review of Predictive Capabilities in Mineral Exploration and Environmental Assessment. *OSF Prepr.* **2025**. [CrossRef]
49. Rousseeuw, P.J.; Van Driessen, K. A Fast Algorithm for the Minimum Covariance Determinant Estimator. *Technometrics* **1999**, *41*, 212–223. [CrossRef]
50. Roberts, D.R.; Bahn, V.; Ciuti, S.; Boyce, M.S.; Elith, J.; Guillera-Arroita, G.; Hauenstein, S.; Lahoz-Monfort, J.J.; Schröder, B.; Thuiller, W.; et al. Cross-Validation Strategies for Data with Temporal, Spatial, Hierarchical, or Phylogenetic Structure. *Ecography* **2017**, *40*, 913–929. [CrossRef]
51. Niculescu-Mizil, A.; Caruana, R. Predicting Good Probabilities with Supervised Learning. In Proceedings of the 22nd International Conference on Machine Learning, Bonn, Germany, 7–11 August 2005; pp. 625–632. [CrossRef]

Disclaimer/Publisher's Note: The statements, opinions and data contained in all publications are solely those of the individual author(s) and contributor(s) and not of MDPI and/or the editor(s). MDPI and/or the editor(s) disclaim responsibility for any injury to people or property resulting from any ideas, methods, instructions or products referred to in the content.